Evidence of correlated incommensurate structural and magnetic order in highly oxygen-doped layered nickelate $Nd_2NiO_{4.23}$

Sumit Ranjan Maity [1,2] Monica Ceretti [3] Lukas Keller [1] Jürg Schefer [1] Bertrand Roessli,[1] Uwe Stuhr [1]
Christof Niedermayer,[1] and Werner Paulus [3]

[1]*Laboratory for Neutron Scattering and Imaging, Paul Scherrer Institut, CH-5232 Villigen, Switzerland*
[2]*Department of Quantum Matter Physics, University of Geneva, 24, Quai Ernest Ansermet, CH-1211 Genève 4, Switzerland*
[3]*ICGM, Univ. Montpellier, CNRS, ENSCM, 34000 Montpellier, France*

$Nd_2NiO_{4+\delta}$ is a nonstoichiometric oxide, crystallizing in the Ruddlesden-Popper-type framework and exhibiting a wide range of oxygen nonstoichiometry δ with a complex structural phase diagram. Excess oxygen atoms insert holes, directly influencing the Ni valence state and associated electronic structure. We report here the existence of a correlated incommensurate structural and antiferromagnetic order below $T_N \approx 150$ K in highly oxygen-doped $Nd_2NiO_{4+\delta}$ with $\delta \approx 0.23$. The crystal and magnetic structures are investigated by polarized and unpolarized single-crystal neutron diffraction studies together with synchrotron x-ray powder diffraction and macroscopic magnetization measurements. Due to the long-range ordering of excess oxygen atoms, the real structure of the compound is incommensurately modulated, represented by $\mathbf{Q}_n = \pm 0.813\mathbf{a}^* \pm 0.519\mathbf{b}^*$ wave vectors. The antiferromagnetic order is characterized by the presence of incommensurate Bragg peaks of type $(h \pm \varepsilon, 0, l/2)$, with h and l being odd-integer numbers and the magnetic incommensurability $\varepsilon \approx 0.36$. The in-plane magnetic correlation length is found to be $\xi_{ab} = 184(1)$ Å but is significantly reduced along the c axis to $\xi_c = 39(2)$ Å, indicating the quasi-two-dimensional nature of the antiferromagnetic correlations. Our study indicates that the excess oxygen atoms nevertheless strongly enhance the magnetic correlations between the NiO_2 planes, resulting in a doubling of the magnetic unit cell along the c axis. In contrast to $Nd_2NiO_{4.1}$, in which the incommensurate periodicity of oxygen and magnetic ordering was found to be identical, the structural and electronic orderings in heavily oxygen-doped $Nd_2NiO_{4.23}$ show two independent modulation vectors. Our study thus unravels a strong correlation between structural and electronic orderings in the highly oxygen-doped $Ln_2NiO_{4+\delta}$ system.

I. INTRODUCTION

The influence of oxygen nonstoichiometry δ on the structural and physical properties of Ruddlesden-Popper (RP) $Ln_2NiO_{4+\delta}$ (Ln = La, Pr, Nd) compounds has been widely investigated since the discovery of superconductivity in isostructural cuprates [1–12]. The crystal structure of these compounds, as depicted in Fig. 1(a), can be described as stacking of $LnNiO_3$-type perovskite layers interspersed with rock-salt-type double LnO layers. The excess oxygen atoms are incorporated between two adjacent LnO layers in the tetrahedral interstitial sites coordinated by four apical oxygen atoms [14]. The excess oxygen content δ can be tuned specifically in the range of $0 \leqslant \delta \leqslant 0.25$ [15].

The doped oxygen atoms inject holes into the system by extracting electrons from the NiO_2 planes, thereby modifying the valence states of Ni^{2+} cations. Hole doping could also be achieved by partially replacing the rare-earth cations with alkaline earth metals such as Sr^{2+}, leading to $Ln_{2-x}Sr_xNiO_{4+\delta}$. On cooling, these holes segregate into narrow channels that act as antiphase domain walls separating antiferromagnetic regions of the Ni^{2+} spins, known as charge-stripe ordered states, in which the spin order is represented by the modulation

vector $\mathbf{Q}_{so} = (\mathbf{Q}_{AF} \pm \varepsilon, 0, 0)$, where $\mathbf{Q}_{AF} = (1, 0, 0)$ is the commensurate antiferromagnetic wave vector observed for the undoped compound, while the charge order is characterized by the modulation vector $\mathbf{Q}_{co} = (\mathbf{Q}_{AF} \pm 2\varepsilon, 0, 0)$ with respect to the pseudotetragonal chemical unit cell [6,16,17]. The magnetic incommensurability ε strongly depends on the hole concentration ($n_h = x$ for Sr-doped systems and 2δ for oxygen-doped systems), and it was shown that ε changes linearly with n_h for $x < 1/2$ [18].

The hole doping via oxygen insertion is not at all similar to Sr doping, as in oxygen-doped systems, in addition to electronic ordering at lower temperatures, the ordering of excess oxygen atoms also occurs at very moderate temperatures ($T \leqslant 800$ K). For example, in $La_2NiO_{4+\delta}$ phases, a one-dimensional stacking of excess oxygen atoms is found for $\delta \leqslant 0.11$ in which intercalated layers of oxygen atoms are spaced periodically along the c axis, and a three-dimensional order is observed for $\delta > 0.145$, while both orders coexist for $0.11 \leqslant \delta \leqslant 0.145$ [19]. The ordering of excess oxygen atoms leads to ordered deformation of NiO_2 planes which provides a modulated potential that can pin the charge stripes to the lattice [19]. Therefore, the excess oxygen atoms and their ordering state both play crucial roles in the nature of charge
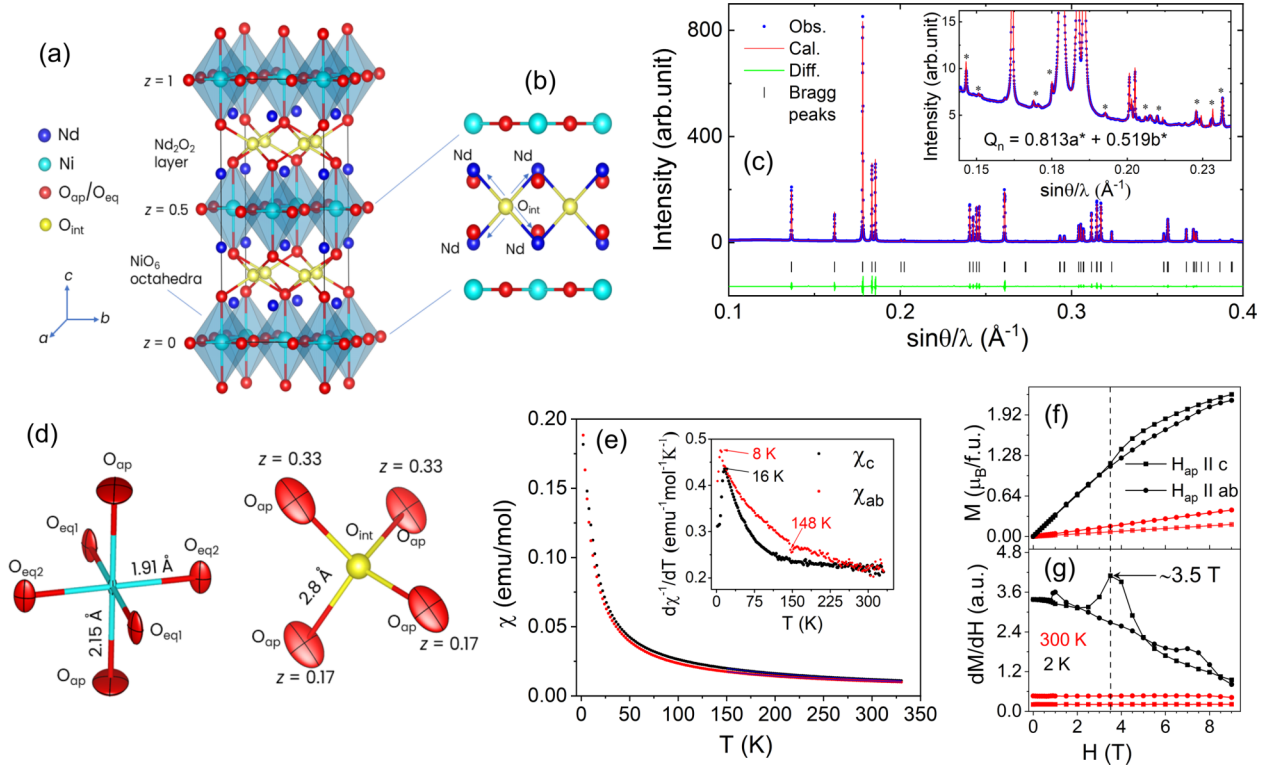
FIG. 1. (a) Idealized layered crystal structure of oxygen-doped $Nd_2NiO_{4.23}$, consisting of interspersed NiO_6 octahedral and Nd_2O_2 rock-salt-type layers. The excess oxygen atoms (O_{int}) occupy the tetrahedral $(\frac{1}{4}, \frac{1}{4}, \frac{1}{4})$ sites coordinated by four apical oxygen atoms. Note that, on average, only one interstitial oxygen atom is present per unit cell. (b) A section of the unit cell in the range $0 \leqslant z \leqslant 0.5$ displaying possible magnetic exchange paths between the Nd_2O_2 layers through the Nd and excess oxygen atoms. The arrows represent the displacement direction of apical oxygen atoms due to Coulombic repulsion by oxygen interstitials. (c) An excerpt of the Rietveld fit of the room temperature synchrotron x-ray powder diffraction data. The inset represents a profile fit of the oxygen superstructure reflections with modulation vectors $Q_n = \pm0.813a^* \pm 0.519b^*$. The details of the indexation process can be found elsewhere [13]. (d) Refined anisotropic thermal ellipsoids of the apical (O_{ap}) and equatorial (O_{eq}) oxygen atoms demonstrating strong structural disorder along the ab plane and the c axis, respectively. The refined bond lengths shown here are obtained from an average structure refinement, while the real structure is strongly distorted, corresponding to a tilt of $\sim25°$ for the NiO_6 octahedra and a shift of about 2 Å of apical oxygen atoms towards [110] with O_{int}-O_{ap} distances of around 2.8 Å instead of 2.13 Å for the nondistorted tetrahedron [10,13]. (e) Temperature-dependent DC magnetic susceptibility curves of the $Nd_2NiO_{4.23}$ single crystal recorded with an applied magnetic field of 1 T parallel to the c axis and the ab plane. The inset represents a first-order temperature derivative of the inverse magnetic susceptibility data. (f) Isothermal magnetization curves measured at 2 and 300 K with magnetic fields applied parallel to the c axis and the ab plane. (g) First-order field derivative of the magnetization data shown in (f).

and spin orders. Single-crystal neutron diffraction measurements of $La_2NiO_{4+\delta}$ compounds illustrated that the nature of the antiferromagnetic order changes from commensurate to stripe at $\delta \approx 0.125$ and the charge order also appears at the same hole concentration [1]. A relationship between the modulation vectors of the charge order and the interstitial order was reported for $La_2NiO_{4.125}$ [6]. Moreover, a correlation between structural and magnetic orderings was recently evidenced for moderately oxygen-doped $Nd_2NiO_{4.10}$ in which identical wave vectors were determined for the ordering of spins and excess oxygen atoms [20].

While the relationship between structural and electronic orders has been comprehensively investigated for low and moderately oxygen-doped systems, it has not been explored much for highly oxygen-doped compounds. Moreover, no evidence of magnetic ordering was found in oxidized $Ln_2NiO_{4+\delta}$ compounds with $\delta \geqslant 0.15$ down to 1.5 K [21,22]. In this work, we investigate the ordering of spins in highly oxygen-doped $Nd_2NiO_{4.23}$ and its correlation to the excess oxygen

atoms by employing neutron and synchrotron x-ray diffraction measurements.

II. EXPERIMENTAL METHODS

The details of powder sample preparation and single-crystal growth of $Nd_2NiO_{4.23}$ are reported elsewhere [23,24]. A single crystal with a size of approximately $2 \times 2 \times 2$ mm^3 was used for all experiments. Synchrotron x-ray powder diffraction (SXRPD) measurements were performed at different temperatures between 5 and 300 K at the Material Sciences (MS) beamline X04SA [$\lambda = 0.564(1)$ Å] at the Swiss Light Source (SLS) of the Paul Scherrer Institute (PSI), Switzerland [25]. Temperature-dependent DC magnetic susceptibility χ measurements on the single crystal were performed using a superconducting quantum interference device magnetometer in the zero-field-cooled (ZFC) configuration by applying 1 T magnetic field parallel (χ_{ab}; $H_{ap} \parallel ab$) and perpendicular (χ_c; $H_{ap} \perp ab$) to the NiO_2 plane.

Direction-dependent isothermal magnetization measurements were performed as a function of applied magnetic fields with decreasing fields from 9 T using a physical property measurement system manufactured by Quantum Design.

Neutron diffraction reciprocal plane maps were performed at different temperatures on DMC at the Swiss spallation neutron source (SINQ), PSI [$\lambda = 2.458(1)$ Å] [26,27]. Selected constant-energy Q scans were carried out at various temperatures on the triple-axis spectrometer EIGER at SINQ, PSI [28,29]. Effective horizontal collimations of 40′-40′-40′-40′ from the reactor to detector were used together with a pyrolytic graphite filter to eliminate neutrons at shorter harmonic wavelengths. Neutrons with an energy of 14.68 meV were selected. Polarized neutron diffraction measurements were performed on the triple-axis spectrometer TASP at SINQ, PSI ($\lambda = 3.14$ Å) equipped with a MUPAD device [30,31]. Field-dependent magnetic measurements were carried out on the cold neutron triple-axis spectrometer RITA-2 at SINQ, PSI, using a 7 T horizontal magnet [32]. At all spectrometers, the neutrons were monochromatized and analyzed by pyrolytic graphite crystals set for the (002) reflection.

III. RESULTS AND DISCUSSION

A. Modulated crystal structure

Room temperature SXRPD data, as shown in Fig. 1(c), reveal a large number of superstructure reflections in addition to the sharp structural Bragg peaks, indicating the long-range ordering of excess oxygen atoms. The positions and intensities of the sharp Bragg peaks are explained by the low-temperature monoclinic structure with the $F112/m$ space group, while most of the superstructure reflections are characterized by modulation vectors $\mathbf{Q}_n = \pm 0.813\mathbf{a}^* \pm 0.519\mathbf{b}^*$, as illustrated in the inset of Fig. 1(c). The details of the refinement and indexation procedure are given elsewhere [13]. No structural transition is observed in the temperature range of 5–300 K, and all the superstructures remain fixed to their positions with no significant intensity changes. The refined lattice parameters of the average F-centered unit cell are determined to be $a = 5.3908(1)$ Å, $b = 5.4510(1)$ Å, $c = 12.3695(2)$ Å, $\alpha = \beta = 90°$, and $\gamma = 90.0764(1)°$ at 300 K. Refined anisotropic thermal ellipsoids of apical and equatorial oxygen atoms are shown in Fig. 1(d), showing large amplitudes along the ab plane and the c axis, respectively. These displacement amplitudes are induced by the excess oxygen atoms and are found to be essential for oxygen mobility close to room temperature within the framework of phonon-assisted oxygen diffusion, as recently demonstrated for oxygen nonstoichiometric oxides with Ruddlesden-Popper structures [10,13,23,33].

B. Magnetic susceptibility

DC magnetic susceptibility curves are shown in Fig. 1(e). No apparent anomaly is observed in χ as a function of temperature since it is strongly dominated by the large, weakly coupled Nd moments while the effects of Ni moments are relatively small. However, three magnetic transitions could easily be distinguished from the temperature derivative of inverse magnetic susceptibility data, as shown in the inset of Fig. 1(e). The first slope change at $T_N \approx 150$ K is

related to the magnetic transition of the Ni sublattice, while the anomaly at 16 K is related to the reorientation of Ni magnetic moments along the crystallographic c axis, as we discuss in the following with neutron diffraction measurements. The anomaly at 8 K corresponds to the onset of magnetic order in the Nd sublattice as reported previously for other $Nd_2NiO_{4+\delta}$ compounds [21,23]. The magnetic susceptibility data were fitted using the Curie-Weiss law given by $\chi = \frac{C}{T-\Theta}$, where C is the Curie constant and Θ is the Curie-Weiss temperature. Since there is a strong contribution of Nd^{3+} crystal field levels below 150 K, the fits were restricted to the temperature range of 150–330 K. The fitting parameters are listed in Table I. A negative Curie-Weiss temperature Θ indicates dominant antiferromagnetic interactions among and between the Ni and Nd magnetic moments at low temperature.

Field-dependent isothermal magnetization curves are shown in Fig. 1(f), while differential magnetization curves are presented in Fig. 1(g). At 300 K, the magnetization curve is linear with the field, indicating a paramagnetic response of the system. However, these magnetization curves at lower temperatures below 10 K in both directions are nonlinear, especially at higher magnetic fields (>3 T). We note that the magnetization curves in both directions are far from the magnetic saturation even at 2 K with 9 T magnetic field. A sharp field-induced magnetic transition is observed at $H_{ap} \approx 3.5$ T $\parallel c$ axis, illustrating the rotation of magnetic moments along this direction under the magnetic field. This transition is clearly visible in the differential magnetization curve shown in Fig. 1(g) and is observed only at $T \leqslant 8$ K, demonstrating its strong correlation to the Nd magnetic moments.

C. Magnetic structure

1. Reciprocal plane maps

The reconstructed neutron diffraction $(h0l)$ reciprocal plane map obtained at 2 K is displayed in Fig. 2(a). Reciprocal h and k directions were arbitrarily assigned since the crystal is twinned on the $(hk0)$ plane. Thus, the following discussion is equally valid for the $(0kl)$ reciprocal plane. Along with sharp structural Bragg peaks, diffuse-type incommensurate magnetic satellites at the $(h \pm \varepsilon, 0, l/2)$ positions are observed, with h and l being odd-integer numbers, where ε is the observed magnetic incommensurability. Representative one-dimensional reciprocal h and l cuts through the (0.64, 0, 1.5) satellite are illustrated in Figs. 2(b) and 2(c), showing the magnetic incommensurability ε to be 0.36 r.l.u. (reciprocal lattice units) with centering at $l = n/2$, where n is an odd-integer number. No temperature dependence in the modulus of ε is observed in our investigated temperature range. The integrated intensity of the (0.64, 0, 1.5) satellite is shown as a function of temperature in Fig. 2(d), demonstrating the appearance of an antiferromagnetic order below 150 K, in accordance with our DC magnetic susceptibility data. The magnetic correlation lengths are obtained from the fitting of reciprocal h and l scans with Lorentzian peak shapes convoluted with a Gaussian-type instrumental resolution function, which was estimated from the fitting of sharp structural Bragg peaks. The magnetic correlation lengths from the Lorentzian peak widths are found to be 184(11) and 39(2) Å in the ab plane (ξ_{ab}) and along the c axis (ξ_c) at 2 K, respectively, suggest-

TABLE I. Magnetic parameters obtained from the fitting of ZFC magnetic susceptibility data with the Curie-Weiss law in the temperature range of 150–330 K.

Crystallographic axis	χ_0 ($\times 10^{-3}$ emu mol^{-1})	C (emu mol K)	Θ (K)	μ_{eff} (units of μ_B)
[001]	0.86	3.89	-54.2	5.57
[110]	2.42	2.74	-31.2	5.87

ing the quasi-two-dimensional nature of antiferromagnetic correlations. The observed correlation length ξ_c is strongly increased compared to the value of 8.4 Å that is found in Sr-doped $Pr_{2-x}Sr_xNiO_4$ ($x \approx 0.5$) [34], demonstrating the role of ordered excess oxygen atoms in the interstitial sites in the interplane magnetic correlation. For the magnetic satellite peak at (0.64, 0, 1.5) (see Fig. S1 of the Supplemental Material [35]), no pronounced change in the peak width is observed in the *ab* plane as a function of temperature, while a clear increase is observed along the *c* axis, i.e., perpendicular to the NiO_2 planes, indicating a substantial decrease in the interplane magnetic correlations on approaching the magnetic transition temperature. We note that the observed magnetic phase in this study seemingly differs from a charge-stripe ordered state that is usually observed in the Sr-doped and moderately oxygen-doped nickelates [17,36,37]. This is justified not only by the absence of magnetic reflections at $l =$ integer numbers but also by the observed ε value, which is determined to be substantially lower than the expected value of $n_h = 2\delta \approx 0.46$ for a charge-stripe ordered state, as previously demonstrated for $La_2NiO_{4+\delta}$ compounds with similar hole concentration.

2. Spherical neutron polarimetry

The diffuse incommensurate reflections observed in our plane maps were previously reported for a highly oxygen-doped $La_2NiO_{4.152}$ compound [38]. However, the origin of these reflections was unclear and speculated to be from an unknown long-range magnetic order. In this study, we employ the spherical neutron polarimetry technique to further explore the origin of these diffuse incommensurate peaks and to estimate the orientation of magnetic moments. This process can be described by a polarization matrix $P_{\alpha\beta}$, which consists of 18 different scattering intensities in the spin-flip $\sigma(\alpha, -\beta)$ and non-spin-flip $\sigma(\alpha, \beta)$ channels in three dimensions [30,39]. The initial and final spin directions are defined by α and β such that

$$P(\alpha, \beta) = \frac{\sigma(\alpha, \beta) - \sigma(\alpha, -\beta)}{\sigma(\alpha, \beta) + \sigma(\alpha, -\beta)},$$

where α and β are x, y, z.

The set of polarization axes is defined as follows: the x direction is parallel to Q, the z direction is perpendicular to the scattering plane, and the y direction completes the right-handed coordinate system. During our measurement, the crystal was mounted on the $(h0l)$ scattering plane with the z axis parallel to the crystallographic b axis of the crystal. Typical scan profiles of the (0.64, 0, 1.5) reflection are plotted in Fig. 2(e) for non-spin-flip (xx) and spin-flip $(x-x)$ configurations. Nearly 10 times larger intensity is detected in the spin-flip channel compared to the non-spin-flip channel, demonstrating the magnetic origin of the diffuse
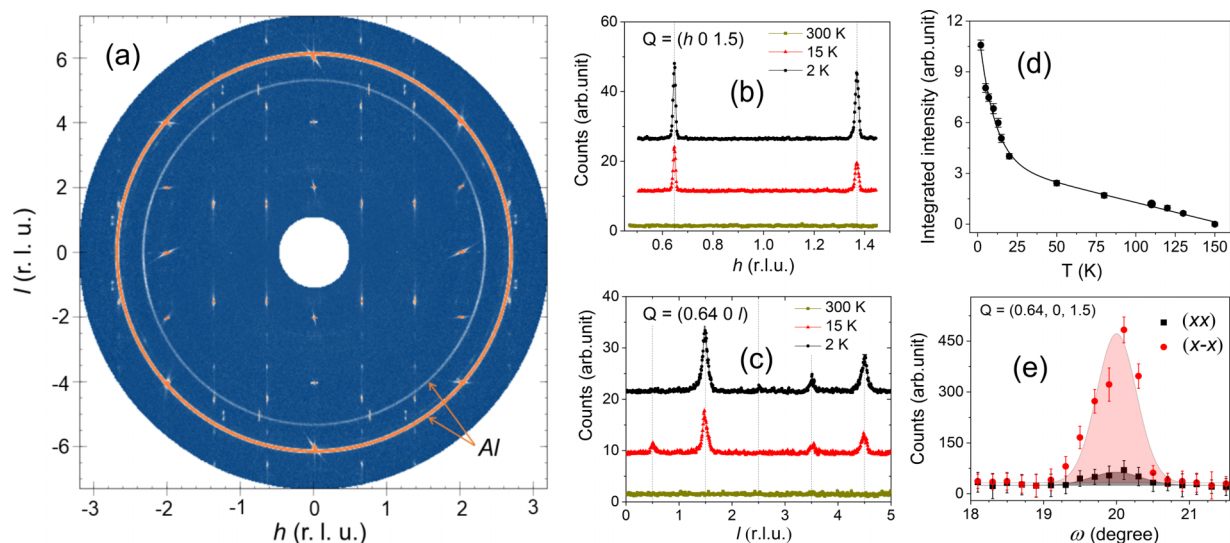

FIG. 2. (a) Neutron diffraction $(h0l)$ reciprocal space plane map of the $Nd_2NiO_{4.23}$ single crystal obtained at 2 K on DMC at SINQ, PSI ($\lambda = 2.458$ Å). Al denotes powder diffraction rings from the aluminum sample holder. (b) and (c) One-dimensional line cuts obtained from the T-dependent plane maps. The scans are for the (0.64, 0, 1.5) magnetic satellite along the reciprocal h and l directions. A constant offset value is applied along the y axis for clarity. (d) The temperature evolution of the integrated intensity of the (0.64, 0, 1.5) magnetic satellite. (e) ω-scan peak profiles obtained for the (0.64, 0, 1.5) reflection in the spin-flip $(x, -x)$ and non-spin-flip (x, x) channels at 2 K on TASP at SINQ, PSI, using MUPAD.

TABLE II. Measured and calculated polarization matrices for $Q_1 = (0.64, 0, 1.5)$ and $Q_2 = (0.64, 0, 4.5)$ magnetic reflections at 2 and 20 K. The G1, G2, and G3 magnetic models were used for matrix elements calculations with the MUFIT program for only the 2 K data. Since integrated intensities were not measured at 20 K, we do not have a magnetic model or calculated matrix elements for this temperature. Matrices were recorded with MUPAD on TASP at SINQ, PSI.

	Measured	Calculated		
		G1	G2	G3
(0.64, 0, 1.5) (2 K)	$\begin{pmatrix} -0.83(6) & -0.12(6) & 0.17(6) \\ 0.12(6) & -0.53(6) & 0.42(6) \\ 0.07(7) & 0.50(6) & 0.46(6) \end{pmatrix}$	$\begin{pmatrix} -0.85 & 0 & 0 \\ 0 & -0.85 & 0 \\ 0 & 0 & 0.85 \end{pmatrix}$	$\begin{pmatrix} -0.85 & 0 & 0 \\ 0 & 0.85 & 0 \\ 0 & 0 & -0.85 \end{pmatrix}$	$\begin{pmatrix} -0.85 & 0 & 0 \\ 0 & -0.85 & 0.58 \\ 0 & 0.58 & 0.85 \end{pmatrix}$
(0.64, 0, 4.5) (2 K)	$\begin{pmatrix} -0.77(4) & 0.05(5) & 0.10(5) \\ -0.02(5) & -0.71(5) & -0.17(5) \\ 0.13(5) & -0.10(5) & 0.68(4) \end{pmatrix}$	$\begin{pmatrix} -0.85 & 0 & 0 \\ 0 & -0.85 & 0 \\ 0 & 0 & 0.85 \end{pmatrix}$	$\begin{pmatrix} -0.85 & 0 & 0 \\ 0 & 0.85 & 0 \\ 0 & 0 & -0.85 \end{pmatrix}$	$\begin{pmatrix} -0.85 & 0 & 0 \\ 0 & -0.85 & -0.18 \\ 0 & -0.18 & 0.85 \end{pmatrix}$
(0.64, 0, 1.5) (20 K)	$\begin{pmatrix} -0.85(5) & -0.06(6) & 0.14(6) \\ 0.11(6) & -0.93(5) & 0.06(6) \\ 0.09(6) & 0.03(6) & 0.83(5) \end{pmatrix}$			

satellites. Complete polarization matrices were recorded at 2 K for two magnetic satellites at $Q_1 = (0.64, 0, 1.5)$ and $Q_2 = (0.64, 0, 4.5)$. Polarization matrices were also measured for two nuclear reflections at $(2, 0, 0)$ and $(0, 0, 2)$ to estimate the polarization efficiency, which was determined to be at 96%. Furthermore, a complete polarization matrix was recorded for a background point at $Q_3 = (0.68, 0, 1.4)$ at 2 K to eliminate the contributions of systematic errors.

3. Group-theory analysis

In this work, we attempt a group-theoretical approach to obtain a magnetic model by using the integrated intensity and polarimetry data for a set of magnetic Bragg peaks. The magnetic propagation vector for the compound can be taken to be $\mathbf{k} = (0.64, 0, 0.5)$. The average structural symmetry of the paramagnetic phase can be assumed to be the $Fmmm$ space group by discarding the subtle monoclinic structural distortion. The program BASIRREPS was used to calculate the possible irreducible magnetic representations (IRs) valid for the propagation vector $\mathbf{k}$. The magnetic representation at the Ni and Nd sites can be decomposed into a direct sum of IRs as $\Gamma_{\text{mag}} = 1\Gamma(1) + 2\Gamma(2)$. The Nd site is split into two orbits related by a center of inversion. All calculated IRs are one-dimensional. The basis vectors ψ for different IRs are calculated using the projection operator technique. The spin distribution of the jth atom can be expressed as the Fourier transform of the linear combination of basis vectors, such that for a single magnetic propagation vector

$$s_j = \sum_n C_n \psi_n \exp(i\mathbf{k}.\mathbf{t}) + \text{c.c.},$$

where the coefficients C_n can be complex, in general. Magnetic moments for the Ni and Nd sites at the (000) and $(00z)$ sites, respectively, are obtained from the basis function calculated for $\Gamma(1)$ and $\Gamma(2)$ resolved along the crystallographic axes as $(0, v, 0)$ and $(u, 0, w)$, respectively. Magnetic structure refinements allow the determination of the free parameters u, v, and w experimentally. That means the magnetic moments are either pointing along the b axis [i.e., in $\Gamma(1)$, hereafter denoted as the G1 model] or lying on the ac plane [i.e., in $\Gamma(2)$, hereafter denoted as the G2 model]. To check which

model represents our data best, least-squares refinements of the integrated intensity data were carried out. Integrated intensities of 18 magnetic reflections were collected with typical ω scans with the crystal oriented on the $(h0l)$ reciprocal plane. In addition, the integrated intensities of six structural Bragg reflections were collected to derive the scale factor for the magnetic structure analysis.

Surprisingly, it was found with the least-squares refinements that the G1 and G2 models provide a similar quality of fit to the observed integrated intensity data (see Fig. S2 in the Supplemental Material [35]). Therefore, we looked into polarization matrices obtained for the magnetic peaks to find the correct model. The recorded matrix elements for two magnetic satellites are presented in Table II after background corrections. We note that at 2 K, for these two satellites, $P(x, x) \neq P(y, y) \neq P(z, z)$ and both $P(x, x)$ and $P(y, y)$ are negative, while $P(z, z)$ is positive and all the other elements are zero within the statistics of the measurements except the mixed term $P(y, z)$ for $(0.64, 0, 1.5)$. These values strongly demonstrate the pure magnetic character of both reflections. However, the $P(y, z)$ component for $(0.64, 0, 1.5)$ arises due to the interference effect between magnetic moments along y and z directions [30].

To determine which magnetic model is consistent with the observed polarization matrices, we calculated the polarization matrices for these two magnetic satellites using both the G1 and G2 magnetic models with the program MUFIT assuming a single-domain sample [40]. Calculated polarization matrices for different models are also presented in Table II. It turns out that the G1 magnetic model is qualitatively in accordance with the observed polarimetry data. In contrast, the G2 model does not match the observed data at all and is excluded by the polarimetry method. However, the presence of the mixed term could not be explained by either magnetic model within the approximation of a single-domain sample. This term may originate from the overlap of scattering intensities from different domains present in the crystal. Two possible types of domains can exist in our single crystal. The first possibility is the presence of structural twin domains. In the case of the $(h0l)$ plane, two structural twins are related by a fourfold rotation matrix about the c axis. The incorporation of
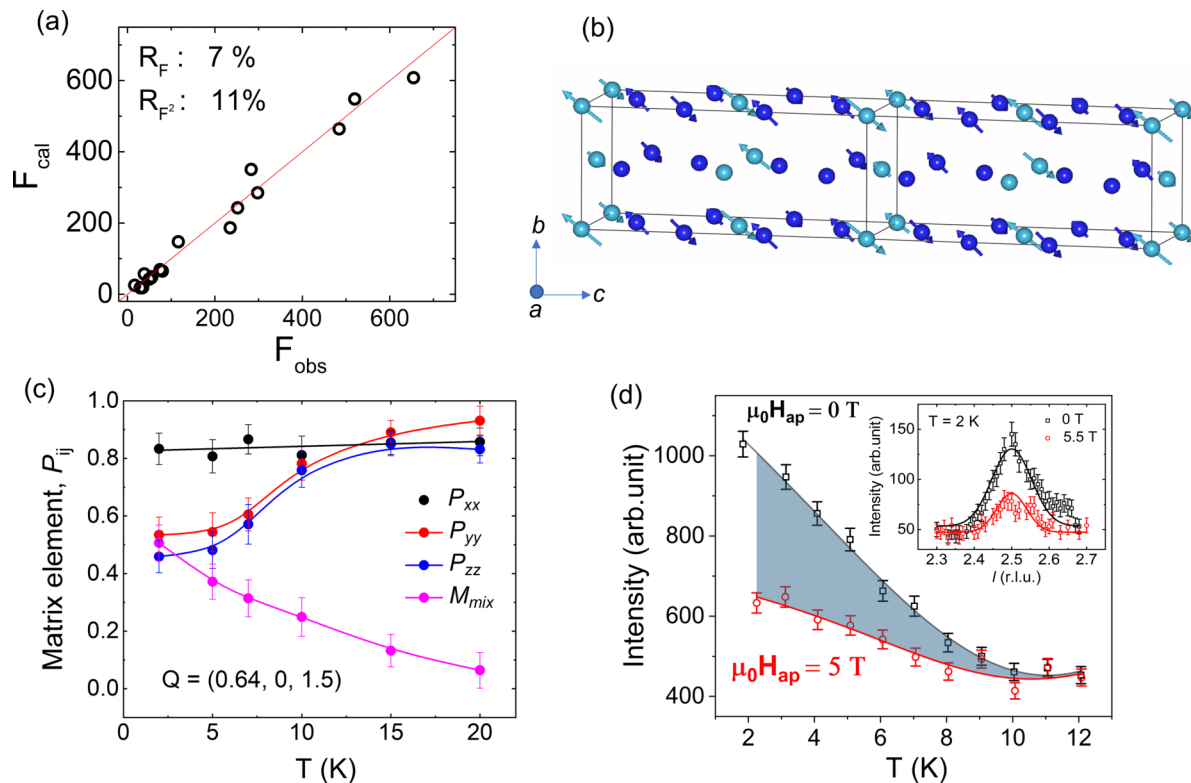
FIG. 3. (a) Plot of calculated and observed magnetic structure factors obtained using the G3 magnetic structure shown in (b). (b) The proposed magnetic structure of $Nd_2NiO_{4.23}$ at 2 K. (c) Temperature evolution of polarization matrix elements for the (0.64, 0, 1.5) reflection. Matrices were recorded with MUPAD on TASP at SINQ, PSI. (d) Temperature evolution of the (0.64, 0, 2.5) magnetic peak intensity with different applied magnetic fields which were applied parallel to the crystallographic c axis. Measurements were performed at RITA II at SINQ, PSI ($E_i = E_f = 3.4$ meV). The inset shows the magnetic field dependence of the corresponding reflection at 2 K. Solid lines are only a guide to the eye.

such structural twins in our calculation does not affect the mixed term at all. The other possibility is the presence of multiple magnetic domains such as configuration K domains and orientation S domains [41]. The scattered intensity at any particular Q is not affected by the presence of multiple K domains. Therefore, these were not included in our calculations. Orientation S domains occur whenever a magnetic structure has lower symmetry than the configurational symmetry. In the present case, two S domains are created by the *x-z* mirror plane. However, the inclusion of these S domains also did not produce the mixed term.

Another possible origin of the mixed term could be the tilting of magnetic moments away from the b axis into the *ac* plane. Our test calculations indeed confirmed that the magnetic interference term can be simulated only if the magnetic moments are slightly tilted away from the b axis into the *ac* plane. In terms of symmetry, the tilting of magnetic moments toward the *ac* plane is not restricted and feasible with the $\Gamma(3)$ representation (hereafter denoted as the G3 model), which can be represented by the linear combination of the G1 and G2 modes. Magnetic moments for the Ni and Nd sites obtained from the basis function calculated for the G3 mode were resolved along the crystallographic axes as (u, v, w), where u, v, and w are free parameters to be determined with refinements. The G3 model fits the data significantly better, as presented in Fig. 3(a), while the refined structure is plotted in Fig. 3(b).

All the least-squares refinement results are presented Table III. With the G3 magnetic model, the calculated polarization matrices for the satellite reflections at Q_1 and Q_2 are in good agreement ($\chi^2 = 7\%$) with the observed polarization matrices. In the final step, the volume fractions of S domains were refined to obtain the best fit ($\chi^2 = 4\%$) with the observed data. Fitted matrices are presented in Table II.

The proposed G3 magnetic model satisfactorily describes the observed magnetic intensities; however, the refined magnetic parameters may contain significant errors since the integrated intensities used in the refinements were obtained from typical ω scans, and due to the diffuse nature of the magnetic peaks these integrated intensities have systematic errors. Moreover, the magnetic form factor of Ni^{2+} ions is used only in the refinements and is assumed to be isotropic, which is not the case because Ni^{3+} ions are also expected to be present in the sample. Furthermore, due to the covalency effect, the magnetic form factor can be strongly anisotropic. In addition, the number of structural and magnetic reflections used in the least-squares refinements and in the polarization analysis is low. Therefore, the absolute values of the magnetic moments obtained may contain significant errors. Nevertheless, our measurements strongly suggest the development of a unique magnetic order in the oxygen-doped $Ln_2NiO_{4+\delta}$ system in the highly doped regime. The interstitial oxygen atoms play a crucial role in the stabilization of such magnetic

TABLE III. Least-squares refinement results for the integrated intensity data obtained for three different magnetic models at 2 K.

	R_F (%)	R_{F2} (%)	Ni site at (0, 0, 0)				Nd site at (0, 0, z)			
			μ_x (units of μ_B)	μ_y (units of μ_B)	μ_z (units of μ_B)	μ_{tot} (units of μ_B)	μ_x (units of μ_B)	μ_y (units of μ_B)	μ_z (units of μ_B)	μ_{tot} (units of μ_B)
G1	11.2	18	0	1.01(9)	0	1.01(9)	0	−0.84(5)	0	0.84(5)
G2	15.8	20.3	0.65(1)	0	−0.13(1)	0.66(2)	0.03(2)	0	0.57(5)	0.57(9)
G3	7	11	−0.44(5)	0.95(9)	−1.03(2)	1.48(6)	0.46(2)	−0.78(5)	0.62(1)	1.09(9)

order along the c axis, along which the magnetic unit cell is doubled.

4. Temperature dependence of the magnetic structure

The temperature evolution of observed matrix elements is plotted in Fig. 3(c) for the $Q_1 = (0.64, 0, 1.5)$ reflection in the temperature range of 2–20 K. The $P(x, x)$ element remains constant over the investigated temperature range, while both the $P(y, y)$ and $P(z, z)$ components increase rapidly with increasing temperature mostly after $T_{N1} = 8$ K. The $P(y, z)$ term simultaneously decreases and goes to zero around 20 K. Referring to the discussion in the previous section, the observed matrix elements at 20 K, as shown in Table II for $(0.64, 0, 1.5)$, demonstrate that the spins are directed along b axis with a very small component along the ac plane. Therefore, a significant part of the ac component of Ni moments is lost in the rearrangement process with increasing temperature beyond T_{N1}. Such a temperature evolution certainly indicates a reorientation of Ni^{2+}/Ni^{3+} spins between 2 and 20 K, which possibly occurs at 16 K according to our magnetic susceptibility data [see Fig. 1(e)]. We should emphasize that the Nd^{3+} ions follow the same magnetic representation as the Ni ions. Thus, the Nd^{3+} ordering at T_{N1} is not expected to induce any spin reorientation. Therefore, such a transition in the Ni sublattice is mainly triggered by short-range magnetic correlations in the Nd sublattice which possibly exist at $T \geqslant T_{N1}$.

5. Magnetic-field-induced transition

The magnetic field dependence effect on the magnetic Bragg peaks was studied by neutron diffraction below 10 K with applied magnetic field $H_{ap} \parallel c$ axis. In Fig. 3(d), we plot the influence of the external magnetic field on the intensity of the magnetic satellite at $(0.64, 0, 2.5)$ at different temperatures. Upon application of the magnetic field $\parallel c$ axis, i.e., perpendicular to the NiO_2 planes, a strong decrease in the peak intensity is observed with $H_{ap} \geqslant 3.5$ T and $T \leqslant 8$ K, in fine agreement with our field-dependent isothermal magnetization data. The peak intensity decreases by 40% upon the application of a magnetic field of 5.5 T at 2 K. The l-scan profiles of the magnetic peak are presented in the inset in Fig. 3(d) for $H_{ap} = 0$ and 5.5 T. We note that the maximum intensity change is observed for this satellite as a function of magnetic field. This particular magnetic peak is weak compared to the other satellites and appears only below $T \approx T_{N1}$ and then rapidly increases with decreasing temperature down to 2 K. Such an evolution manifests its correlation to the ordering of Nd^{3+} ions. Therefore, the field-induced effect is possibly due to the strong contribution of Nd^{3+} magnetic moments to the magnetic structure factor of this magnetic satellite and the rotation of Nd^{3+} magnetic moments under the magnetic field. Thus, our neutron diffraction data together with magnetization measurements reveal a strong magnetic-field-induced effect of $Nd_2NiO_{4.23}$; however, our present neutron diffraction data are not enough for quantitative analysis of such changes in the magnetic structure.

IV. CONCLUSIONS

In summary, the crystal structure of $Nd_2NiO_{4.23}$ was revealed to be three-dimensionally modulated, owing to the long-range ordering of excess oxygen atoms in the investigated temperature range of 2–330 K. The oxygen ordering, essentially established within the *ab* plane, also involves an important electronic coupling along [001], as it directly strengthens the bonding throughout the Nd_2O_2 layer. The important consequence then is the establishment of a magnetic exchange path along the Ni-O_{ap}-O_{int}-O_{ap}-Ni atoms, with the Ni-Ni distances between two layers being 6.75 and 7.28 Å. An enhanced magnetic correlation between the NiO_2 planes was also indicated by a doubling of the magnetic unit cell along the *c* direction. The antiferromagnetic order of the Ni sublattice is evidenced below $T_N \approx 150$ K, while the magnetic order of Nd^{3+} is detected below 8 K. The incommensurate magnetic structure is characterized by the magnetic satellites at $(h \pm \varepsilon, 0, l/2)$, with h and l being odd-integer numbers with magnetic incommensurability, $\varepsilon \approx 0.36$. The observed magnetic ordering is thus substantially different from the stripe spin order usually observed in hole-doped RP nickelates following the rare earth substitution by Sr. Therefore, the incommensurate component of the structural modulation vector is essentially in the *ab* plane, while the incommensurate magnetic component points along the *c* axis. Thus, the highly oxygen-doped $Nd_2NiO_{4.23}$ presents an interesting scenario in which long-range incommensurate ordering of interstitial oxygen atoms and a long-range incommensurate antiferromagnetic order coexist down to 2 K. We revealed that the magnetic correlation along the *c* axis is mediated through the excess oxygen atoms at the interstitial sites, establishing a stronger magnetic correlation between the NiO_2 planes and thereby doubling the magnetic unit cell along this direction. This is certainly a promising perspective, as it could allow us to achieve complex magnetic ordering as a consequence of long-range oxygen ordering; the latter can then be tuned by the excess oxygen stoichiometry.

[1] J. M. Tranquada, Y. Kong, J. E. Lorenzo, D. J. Buttrey, D. E. Rice, and V. Sachan, Oxygen intercalation, stage ordering, and phase separation in $La_2NiO_{4+\delta}$ with $0.05 \leqslant \delta \leqslant 0.11$, Phys. Rev. B **50**, 6340 (1994).

[2] N. Poirot, C. Allançon, P. Odier, P. Simon, J. Bassat, and J. Loup, Magnetic properties of $La_2NiO_{4.16}$ and $La_{12-x}Pr_xNiO_{4+\delta}$, J. Solid State Chem. **138**, 260 (1998).

[3] J. M. Tranquada, D. J. Buttrey, J. E. Lorenzo, and V. Sachan, Ordering of holes and spins in $La_2NiO_{4.125}$ and $La_{1.8}Sr_{0.2}NiO_4$, Phys. B (Amsterdam, Neth.) **213-214**, 69 (1995).

[4] X. Batlle, X. Obradors, M. J. Sayagues, M. Vallet, and J. Gonzalez-Calbet, Weak ferromagnetism and magnetic interactions in La_2NiO_4, J. Phys.: Condens. Matter **4**, 487 (1992).

[5] A. Demourgues, P. Dordor, J.-P. Doumerc, J.-C. Grenier, E. Marquestaut, M. Pouchard, A. Villesuzanne, and A. Wattiaux, Transport and magnetic properties of $La_2NiO_{4+\delta}$ ($0 \leqslant \delta \leqslant 0.25$), J. Solid State Chem. **124**, 199 (1996).

[6] P. Wochner, J. M. Tranquada, D. J. Buttrey, and V. Sachan, Neutron-diffraction study of stripe order in La_2NiO_4 with $\delta = 2/15$, Phys. Rev. B **57**, 1066 (1998).

[7] K. Nakajima, Y. Endoh, S. Hosoya, J. Wada, D. Welz, H. M. Mayer, H. A. Graf, and M. Steiner, Neutron scattering study of oxygen ordering and magnetic correlations in $La_2NiO_{4.11}$ and $La_2NiO_{4.125}$, J. Phys. Soc. Jpn. **66**, 809 (1997).

[8] W. Paulus, A. Cousson, G. Dhalenne, J. Berthon, A. Revcolevschi, S. Hosoya, W. Treutmann, G. Heger, and R. Le Toquin, Neutron diffraction studies of stoichiometric and oxygen intercalated La_2NiO_4 single crystals, Solid State Sci. **4**, 565 (2002).

[9] J. M. Bassat, M. Burriel, O. Wahyudi, R. Castaing, M. Ceretti, P. Veber, I. Weill, A. Villesuzanne, J.-C. Grenier, W. Paulus, and J. A. Kilner, Anisotropic oxygen diffusion properties in $Pr_2NiO_{4+\delta}$ and $Nd_2NiO_{4+\delta}$ single crystals, J. Phys. Chem. C **117**, 26466 (2013).

[10] M. Ceretti, O. Wahyudi, A. Cousson, A. Villesuzanne, M. Meven, B. Pedersen, J. M. Bassat, and W. Paulus, Low temperature oxygen diffusion mechanisms in $Nd_2NiO_{4+\delta}$ and $Pr_2NiO_{4+\delta}$ via large anharmonic displacements, explored by single crystal neutron diffraction, J. Mater. Chem. A **3**, 21140 (2015).

[11] A. Perrichon, A. Piovano, M. Boehm, M. Zbiri, M. Johnson, H. Schober, M. Ceretti, and W. Paulus, Lattice dynamics modified by excess oxygen in $Nd_2NiO_{4+\delta}$: Triggering low-temperature oxygen diffusion, J. Phys. Chem. C **119**, 1557 (2015).

[12] A. A. Nikonov and O. E. Parfenov, Two-dimensional quantum ferromagnet, magnetic chains, and oxygen ordering in $La_2NiO_{4.125}$ single crystals, JETP Lett. **78**, 25 (2003).

[13] S. R. Maity, M. Ceretti, R. De Barros, L. Keller, J. Schefer, A. Cervellino, J. A. Rodríguez Velamazan, and W. Paulus, Large-scale oxygen order phase transitions and fast ordering kinetics at moderate temperatures in $Nd_2NiO_{4+\delta}$ electrodes, Mater. Adv. **4**, 651 (2023).

[14] J. D. Jorgensen, B. Dabrowski, S. Pei, D. R. Richards, and D. G. Hinks, Structure of the interstitial oxygen defect in $La_2NiO_{4+\delta}$, Phys. Rev. B **40**, 2187 (1989).

[15] S. Bhavaraju, J. F. DiCarlo, D. P. Scarfe, I. Yazdi, and A. J. Jacobson, Electrochemical intercalation of oxygen in Nd_2NiO_{4+x} ($0 \leqslant x \leqslant 0.18$) at 298 K, Chem. Mater. **6**, 2172 (1994).

[16] J. M. Tranquada, Stripe correlations of spins and holes in cuprates and nickelates, Ferroelectrics **177**, 43 (1996).

[17] J. M. Tranquada, B. J. Sternlieb, J. D. Axe, Y. Nakamura, and S. Uchida, Evidence for stripe correlations of spins and holes in copper oxide superconductors, Nature (London) **375**, 561 (1995).

[18] H. Yoshizawa, T. Kakeshita, R. Kajimoto, T. Tanabe, T. Katsufuji, and Y. Tokura, Stripe order at low temperatures in $La_{2-x}Sr_xNiO_4$ with $0.289 \lesssim \delta \lesssim 0.5$, Phys. Rev. B **61**, R854 (2000).

[19] H. L. Zhang, X. S. Wu, C. S. Chen, and W. Liu, Excess oxygen ordering in the $La_2NiO_{4+\delta}$ system studied by low-frequency internal friction, Phys. Rev. B **71**, 064422 (2005).

[20] S. R. Maity, M. Ceretti, L. Keller, J. Schefer, M. Meven, E. Pomjakushina, and W. Paulus, Interdependent scaling of long-range oxygen and magnetic ordering in non-stoichiometric $Nd_2NiO_{4.10}$, Phys. Rev. Mater. **5**, 014401 (2021).

[21] J Rodríguez-Carvajal, M. T. Fernández-Díaz, J. L. Martínez, F. Fernández, and R. Saez-Puche, Structural phase transitions and three-dimensional magnetic ordering in the Nd_2NiO_4 oxide, Europhys. Lett. **11**, 261 (1990).

[22] J. Rodriguez-Carvajal, M. T. Fernandez-Diaz, and J. L. Martinez, Neutron diffraction study on structural and magnetic properties of La_2NiO_4, J. Phys.: Condens. Matter **3**, 3215 (1991).

[23] S. R. Maity, M. Ceretti, L. Keller, J. Schefer, T. Shang, E. Pomjakushina, M. Meven, D. Sheptyakov, A. Cervellino, and W. Paulus, Structural disorder and magnetic correlations driven by oxygen doping in $Nd_2NiO_{4+\delta}$ ($\delta \sim 0.11$), Phys. Rev. Mater. **3**, 083604 (2019).

[24] O. Wahyudi, M. Ceretti, I. Weill, A. Cousson, F. Weill, M. Meven, M. Guerre, A. Villesuzanne, J.-M. Bassat, and W. Paulus, Growth of high quality single crystals of strontium doped (Nd,Pr)-nickelates, $Nd_{2-x}Sr_xNiO_{4+\delta}$ and $Pr_{2-x}Sr_xNiO_{4+\delta}$, CrystEngComm **17**, 6278 (2015).

[25] P. R. Willmott *et al.*, The Materials Science beamline upgrade at the Swiss Light Source, J. Synchrotron Radiat. **20**, 667 (2013).

[26] J. Schefer, P. Fischer, H. Heer, A. Isacson, M. Koch, and R. Thut, A versatile double-axis multicounter neutron powder diffractometer, Nucl. Instrum. Methods Phys. Res., Sect. A **288**, 477 (1990).

[27] Cold neutron powder diffractometer DMC, https://www.psi.ch/sinq/dmc/.

[28] U. Stuhr, B. Roessli, S. Gvasaliya, H. M. Rønnow, U. Filges, D. Graf, A. Bollhalder, D. Hohl, R. Bürge, M. Schild, L. Holitzner, C. Kaegi, P. Keller, and T. Mühlebach, The thermal triple-axis-spectrometer EIGER at the continuous spallation source SINQ, Nucl. Instrum. Methods Phys. Res., Sect. A **853**, 16 (2017).

[29] EIGER: Thermal neutron triple-axis-spectrometer, https://www.psi.ch/en/sinq/eiger.

[30] M. Janoschek, S. Klimko, R. Gähler, B. Roessli, and P. Böni, Spherical neutron polarimetry with MuPAD, Phys. B (Amsterdam, Neth.) **397**, 125 (2007).

[31] TASP: Cold neutron triple-axis spectrometer, https://www.psi.ch/en/sinq/tasp.

[32] K. Lefmann, D. F. McMorrow, H. M. Rønnow, K. Nielsen, K. N. Clausen, B. Lake, and G. Aeppli, Added flexibility in triple axis spectrometers: The two RITAs at Risø, Phys. B (Amsterdam, Neth.) **283**, 343 (2000).

[33] M. Ceretti, O. Wahyudi, G. André, M. Meven, A. Villesuzanne, and W. Paulus, $(Nd/Pr)_2NiO_{4+\delta}$: Reaction intermediates and redox behavior explored by in situ neutron powder diffraction during electrochemical oxygen intercalation, Inorg. Chem. **57**, 4657 (2018).

[34] R. Dutta, A. Maity, A. Marsicano, J. R. Stewart, M. Opel, and W. Paulus, Direct evidence for anisotropic three-dimensional magnetic excitations in a hole-doped antiferromagnet, Phys. Rev. B **102**, 165130 (2020).

[35] See Supplemental Material at http://link.aps.org/supplemental/10.1103/PhysRevMaterials.7.024412 for an analysis of the temperature dependence of magnetic peak widths for the satellite at $(0.64, 0, 0.5)$ and possible magnetic structures of $Nd_2NiO_{4.23}$ as obtained from the single-crystal neutron diffraction data.

[36] P. G. Freeman, A. T. Boothroyd, D. Prabhakaran, D. González, and M. Enderle, Spin reorientation transition in the incommensurate stripe-ordered phase of $La_{3/2}Sr_{1/2}NiO_4$, Phys. Rev. B **66**, 212405 (2002).

[37] P. G. Freeman, A. T. Boothroyd, D. Prabhakaran, M. Enderle, and C. Niedermayer, Stripe order and magnetic transitions in $La_{2-x}Sr_xNiO_4$, Phys. Rev. B **70**, 024413 (2004).

[38] K. Yamada, T. Omata, K. Nakajima, Y. Endoh, and S. Hosoya, Incommensurate magnetic correlations in $La_2NiO_{4.125}$, Magnetic phase diagram and two-dimensional hole-order, Phys. C (Amsterdam, Neth.) **221**, 355 (1994).

[39] M. Blume, Polarization effects in the magnetic elastic scattering of slow neutrons, Phys. Rev. **130**, 1670 (1963).

[40] A. Poole and B. Roessli, Analysis of neutron polarimetry data using MuFit, J. Phys.: Conf. Ser. **340**, 012017 (2012).

[41] P. Brown, Magnetic structure studied with zero-field polarimetry, Phys. B (Amsterdam, Neth.) **192**, 14 (1993).